Progress In Electromagnetics Research C, Vol. 161, 226–238, 2025

PIER C

(Received 11 September 2025, Accepted 31 October 2025, Scheduled 13 November 2025)

A Compact Dual-Polarized Hexagonal Loop Antenna for Underwater Communication with Experimental Validation of Polarization Diversity

Joko Suryana[1,*], Ali Rhomadoni[2], and Ahmad Izzuddin[1]

[1] *Radio Telecommunication and Microwave Laboratory, Bandung Institute of Technology, Indonesia*
[2] *Telematics Laboratory, Bandung Institute of Technology, Indonesia*

ABSTRACT: Underwater electromagnetic communication is severely limited by the high permittivity and conductivity of water, which cause strong attenuation at higher frequencies. To overcome this challenge, a compact dual-polarized hexagonal loop antenna is proposed and experimentally validated for low-frequency underwater communication at 40–45 MHz. The antenna, fabricated on FR-4 and sealed with epoxy resin, eliminates bulky waterproof housings while ensuring stable impedance performance with a measured return loss better than −10 dB. Experiments conducted in freshwater confirm the effectiveness of polarization diversity, achieving an average received-power improvement of 4.59 dB under maximal-ratio combining. These results demonstrate, for the first time, the feasibility of a practical dual-polarized hexagonal loop design for robust, low-frequency underwater communication systems and future MIMO-like implementations.

1. INTRODUCTION

Underwater wireless communication plays a vital role in modern marine applications such as environmental monitoring, autonomous underwater vehicles (AUVs), and submerged sensor networks. Despite its importance, underwater communication remains challenging due to the high attenuation of water that possesses both high permittivity and high conductivity. This property significantly impedes the propagation of electromagnetic (EM) waves, especially at high frequencies. Therefore, the use of the lowest possible frequency combined with good antenna design in underwater environments is very important for underwater communications.

Underwater RF antenna designs have gained increasing attention over the past decade, yet most implementations remain limited to single polarization. Table 1 summarizes representative studies from the period. Although various configurations have been explored, including dipoles, patch antennas, and wire loops, dual polarizations are still uncommon. A notable recent work by Hasaba et al. [1] implemented a large octagonal loop antenna with a diameter of approximately 2 m as part of a Wavelet-OFDM system for AUVs operating in seawater. While the antenna was not dual-polarized, its robust performance, demonstrating a data rate up to 6.8 Mbps over several meters, highlighting the effectiveness of magnetically coupled loop antennas in lossy underwater environments. This performance could be further improved by employing a dualpolarized loop antenna.

Dual-polarized antennas are conventionally implemented using square or rectangular patch structures with orthogonal feeding techniques, or by arranging two dipole elements in a mutually orthogonal configuration. These approaches are widely adopted in terrestrial and aerial communication systems due to their well-understood polarization behavior and ease of integration. However, the usage of dual-polarization loop antenna has not yet been explored.

Loop antennas, while being traditionally single-polarized, offer promising alternatives due to their symmetrical current distribution and magnetic field dominance, particularly beneficial in electrically small or lossy environments. However, the integration of dual-polarization capability into loop geometries remains largely unexplored. Among various loop shapes, hexagonal loop stands out for its structural rigidity and potential for polarization manipulation via orthogonal feeding. Despite these advantages, limited research has addressed the dual-polarization potential of hexagonal loop antennas, especially at low frequencies or in underwater scenarios.

Research on hexagonal loop antennas has evolved from theoretical modeling to practical performance evaluation. Lim etal. [2] provided foundational insights through Method of Mome nts (MoM) analysis on electrically large thin hexagonal loop antennas ($C = 3\lambda$), where C is the hexagonal loop circumference, exploring both near- and far-field behaviors. However, their study was purely theoretical and lacked validation via full-wave simulations or physical measurements. Patel et al. [3] later conducted a comparative study based on Numerical Electromagnetics Code (NEC) simulation software between hexagonal ($C = 1.1\lambda$) and circular loop antennas using thick wire elements, reporting differences in radiation patterns and return losses across the ultra-high frequency

---

* Corresponding author: Joko Suryana (joko@itb.ac.id).

doi:10.2528/PIERC25091101

Published by THE ELECTROMAGNETIC ACADEMY

TABLE 1. Recent underwater antenna research (last 10 years).

Ref.	Antenna Type	Freq. (MHz)	Features	Advantages	Limitations
[4]	Dipole	400	Circularly polarized underwater antenna, experimentally verified in a water tank.	Reduces polarization mismatch losses, suitable for high-frequency underwater applications.	Lacks dual-polarization or MIMO compatibility, potentially limiting diversity gains.
[5]	Patch	100–1000	Designed for underwater communications, fabricated for practical use.	Wide frequency range, robust for various underwater applications.	Single-polarization design, no support for polarization diversity, potentially bulky.
[6]	Triangular Monopole	700–1000	Designed for LoRa communication, includes underwater and water surface applications.	Supports long-range communication, versatile for surface and underwater use.	Single-polarization, high-frequency operation increases attenuation in water.
[7]	Wire Loop	39	Optimized for underwater radio communications, low-frequency design.	Low attenuation at 39 MHz, suitable for freshwater environments.	Single-polarization, lacks diversity features, may require larger dimensions.
[9]	J-Dipole	40	J-pole configuration analyzed for underwater communications.	Simple design, effective at low frequencies for reduced attenuation.	No dual-polarization, limited to single-polarization performance, complex waterproofing needs.
[8]	Wire Loop	6.78	Designed for underwater telemetry, low-frequency operation.	Very low frequency reduces signal attenuation, suitable for deep-water applications.	Single-polarization, large physical size due to low frequency, limited bandwidth.
[10]	Monopole Planar	433	Real-time underwater communication with antenna diversity for swimming training.	Supports real-time applications, incorporates diversity for improved reliability.	Single-polarization, high-frequency operation may face higher attenuation, specific to niche applications.
[1]	Hexagonal Loop (Octagonal frame)	0.125–1.75	Wavelet-OFDM underwater system using large single-turn loop integrated with AUV.	Demonstrated 6.8 Mbps communication over several meters in seawater, robust to misalignment.	Single polarization only, large size (2m loop), not optimized for polarization diversity.

(UHF). This work also concluded that hexagonal loop antenna has wider bandwidth than circular loop antenna. However, their work did not address polarization behavior or include experimental radiation measurements.

While previous studies have explored various underwater antenna configurations, most have focused on achieving impedance matching or bandwidth enhancement rather than optimizing polarization diversity and structural compactness. Dipole- and patch-based designs [4–6] provided stable radiation but were limited to single polarization, restricting their suitability for diversity or multiple-input multiple-output (MIMO)-like applications. Loop antennas such as those reported in [1, 7, 8] achieved efficient low-frequency operation but required large dimensions or complex waterproof housings. Similarly, compact monopole and J-pole variants [9, 10] offered simple fabrication yet suffered from narrow bandwidth and high inter-polarization correlation. In contrast, the proposed dual-polarized hexagonal loop antenna integrates compact geometry (1.5λ circumference), orthogonal polarization capability, and epoxy-sealed FR-4 implementation that eliminates the need for bulky housings. Moreover, this work provides the first experimental validation of polarization diversity in freshwater, demonstrating measurable diversity gain and independence between polarization ports.

Two key research gaps remain: (1) Although dual-polarized antennas have been extensively developed for terrestrial applications [11–14], no prior study has explored the design of a hexagonal loop antenna with dual polarizations for underwater communication; and (2) While circular polarization designs [4] can mitigate multipath effects in underwater environments, they do not provide orthogonal mode separation and are not suitable for MIMO systems with polarization diversity. In addition, (3) the existing method of isolating loop antenna conductors from water, such as enclosing the wire inside a pipe as in [1], was relatively complex, whereas in this study we propose a simpler approach using epoxy resin, a material commonly used in printed circuit board (PCB) fabrication. Our proposed dual-polarization hexagonal loop implementation directly addresses these three gaps by combining the unique geometry of the hexagonal loop with polarization diversity and introducing a practical isolation technique for reliable underwater communication systems.

To the best of our knowledge, no previous work has experimentally validated a compact hexagonal dual-polarized antenna in freshwater, supported by both EM simulation and comprehensive S-parameter, radiation, and received power characterizations. This study also addresses these critical gaps.

In this work, the antenna was fabricated on a standard FR-4 substrate and coated with a thin epoxy resin to avoid direct contact with the surrounding medium. Freshwater was used as the test environment to provide a controlled, low-conductivity environment that allows an accurate evaluation of the antenna's electromagnetic behavior, particularly in terms of polarization and isolation characteristics, without the excessive losses commonly encountered in saline environments. The findings here may serve as a foundation for future adaptations to seawater conditions through material and impedance optimization.

The primary contributions of this study are as follows:

- Design and realization of a compact hexagonal loop antenna with dual polarizations for underwater communication.
- An easy fabrication process using FR-4 and epoxy resin sealing, eliminating the need for bulky waterproof housings.
- Experimental validation of polarization diversity effectiveness via received power-level statistical distribution analysis using diversity-combining techniques (SC, EGC, MRC).

The remainder of this paper is organized as follows. Section 2 provides details of antenna design and analysis, including propagation model, hexagonal geometry, dual-polarization theory, and EM simulation results. Section 3 describes the measurement setup, covering S-parameter evaluation, radiation pattern measurements, and dual-polarization test procedure. Section 4 presents and discusses the experimental results, including S-parameter analysis, far-field radiation patterns, and polarization diversity performance based on received power level distribution. Finally, Section 5 concludes the paper and summarizes the main findings.

2. ANTENNA DESIGN AND ANALYSIS

2.1. Underwater Radio Propagation

For underwater communication applications, the operating frequency should be selected as low as possible to reduce signal attenuation. In this study, 45 MHz is chosen as the center frequency for antenna design, offering a balance between practical antenna dimensions and effective wave propagation in freshwater environments, as supported by [7, 15].

The propagation characteristics of electromagnetic waves in a lossy medium are described by the complex propagation constant γ, as expressed in Equation (1):

$$\gamma = \alpha + j\beta \tag{1}$$

where α is the attenuation constant (Np/m), and β is the phase constant (rad/m). The attenuation and phase constants are given by:

$$\alpha = \omega\sqrt{\frac{\mu\epsilon}{2}\left(\sqrt{1+\left(\frac{\sigma}{\omega\epsilon}\right)^2}-1\right)} \tag{2}$$

$$\beta = \omega\sqrt{\frac{\mu\epsilon}{2}\left(\sqrt{1+\left(\frac{\sigma}{\omega\epsilon}\right)^2}+1\right)} \tag{3}$$

where ω is the angular frequency (rad/s), μ the permeability (H/m), ϵ the permittivity (F/m), and σ the conductivity (S/m).

Freshwater typically exhibits a conductivity (σ) in the range of 0.005–0.05 S/m, while seawater has a much higher conductivity of approximately 4 S/m [16]. In this study, freshwater with a conductivity of 0.0487 S/m and a relative permittivity of $\varepsilon_r = 81$ is used, based on reported values in [7]. The low conductivity makes freshwater a lower-loss medium for electromagnetic wave propagation at MHz frequencies than seawater, where attenuation becomes too high to be practical.

Equations (2) and (3) are evaluated using $\omega = 2\pi f$ and $\epsilon = \varepsilon_0\varepsilon_r$. A key parameter for classifying the medium is $\frac{\sigma}{\omega\epsilon}$, which distinguishes conductive ($\gg 1$) from dielectric ($\ll 1$) behavior [17]. At 45 MHz in freshwater, this value is approximately 0.24, indicating that wave-like propagation is supported, and attenuation remains moderate.

The wavelength in the medium is given by:

$$\lambda = \frac{2\pi}{\beta} \tag{4}$$

The calculated attenuation constant α is approximately 1.01 Np/m, and the phase constant β is 8.55 rad/m. These values yield a wavelength of approximately 0.735 m in freshwater according to Equation (4). This wavelength permits the construction of a loop antenna with a circumference of 1.5λ (around 1.10 m), which remains within the fabrication constraint of a 600 mm diameter for a folded or compact design.

The theoretical formulations in Equations (2)–(4) establish a direct foundation for determining both the operating frequency range and physical scale of the proposed antenna. Attenuation constant α represents the exponential decay of wave amplitude in the medium and thus governs the feasible communication range rather than the antenna geometry. At 45 MHz, the calculated $\alpha \approx 1.01$ Np/m means that the field amplitude decreases to $e^{-1.01} \approx 0.36$ (about 36% of its initial value) after one meter of propagation. This corresponds to roughly 13% of the transmitted power being retained, indicating a moderate loss that remains acceptable for short-range underwater communication. Therefore, the attenuation level justifies the use of the 40–45 MHz band, where signal degradation is limited compared to higher frequencies.

In contrast, phase constant β directly defines the wavelength $\lambda = 2\pi/\beta$, which determines the physical dimensions required for resonance. The resulting wavelength about 0.735 m in freshwater provides a practical loop circumference of 1.5λ (approximately 1.10 m), which fits within the mechanical fabrication constraint of a 600 mm folded diameter. Consequently, while α constrains the feasible operating distance and motivates the frequency selection due to acceptable attenuation, β dictates the geometric configuration necessary to achieve resonant and efficient radiation in the underwater environment.

2.2. Antenna Geometry and Feeding Configuration

The hexagonal loop antenna in this study was designed with a total circumference of 1.5λ as shown in Figure 1, following the

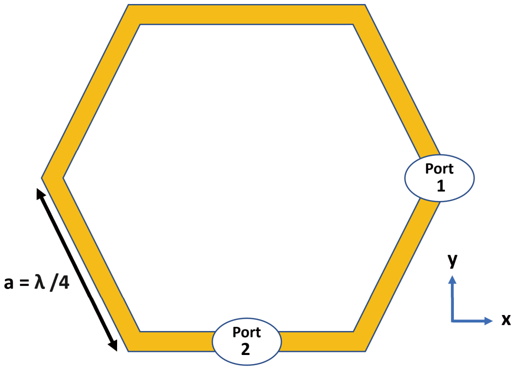

FIGURE 1. Geometry of the proposed dual-port hexagonal loop antenna showing orthogonal excitation ports. Each port excites a polarization orthogonal to the other, and the loop side length is designed as approximately $a = \lambda/4$.

theoretical framework presented by Lim et al. [2]. This length is known to obtain high directivity for loop antennas. The antenna supports two independent feed configurations: one located at the center of a hexagonal edge and the other near the corner, enabling the implementation of orthogonal field orientations. The two ports realize orthogonal linear polarizations. Although a 90° phasing could synthesize circular polarization, in this work the ports are excited independently to evaluate dual linear polarizations and polarization diversity.

As discussed in Balanis' Antenna Theory [18], a loop antenna with a circumference of approximately 1.5λ achieves its maximum directivity. This configuration yields a high input impedance (hundreds of ohms), so an impedance-matching network to 50 Ω is typically required. The design can be simplified by designing the radiation resistance to be as close as possible to 50 Ω. To address this, the loop conductor width should be thicker, which reduces the loop radiation resistance. The dimensionless parameter $\Omega = 2\ln\left(\frac{2\pi a}{b}\right)$ serves to estimate the radiation resistance, where a is the loop radius, and b is the conductor radius.

2.3. Antenna Design in EM Simulation Software

This section presents the detailed design of the compact dual-polarized hexagonal loop antenna. The antenna consists of a copper trace printed on a single-layer FR-4 substrate with a relative permittivity ε_r of 4.3–4.6 and a thickness of 1.6 mm, as specified by the manufacturer's datasheet.

To prevent direct contact between the copper conductor and water, the antenna is coated with an ultra-thin epoxy resin layer with ε_r of 4, as shown in Figure 2. This protective layer not only ensures that there is no direct contact between the conductor element of loop antenna and water, but also extends the life of the antenna by reducing corrosion caused by substances dissolved in water [19].

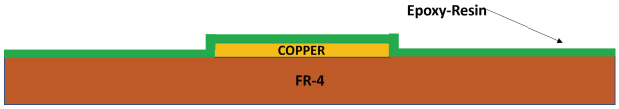

FIGURE 2. Cross-sectional view of the printed hexagonal loop antenna illustrating the copper trace on FR-4 substrate and the ultra-thin (≈ 0.01 mm) epoxy-resin coating used for waterproof sealing.

Figure 3 illustrates the hexagonal geometry of the antenna modeled in the simulation. The geometric parameters are detailed in Table 2. A feed arm of length L_{Feed} serves to connect the loop to an SMA connector. Port 1 (bottom) and Port 2 (side) are designed to have feed lines of the same length, ensuring minimal phase difference. The loop thickness T_{Loop} and feed line width W_{Feed} are designed to be equal, as both dimensions impact the antenna's radiation resistance R_r.

TABLE 2. Geometric parameters of the hexagonal loop antenna.

Parameter	Value (mm)	Description
a	185	Side length of hexagon
R_{Loop}	185	Effective loop radius
T_{Loop}	8.12	Loop conductor width
L_{Feed}	24	Feed arm length
G_{Feed}	10	Feed gap
W_{Feed}	8.12	Feed line width

Figure 4 presents the simulated S-parameter responses of the antenna, including the return loss at Port 1 and Port 2 (S_{11}, S_{22}). The return loss values remain below -10 dB across 34–56 MHz, confirming that the antenna maintains proper impedance matching and operates effectively as both a transmitter and a receiver within this frequency range. However, a closer examination shows that the return loss characteristics at Port 1 and Port 2 are not completely identical. The return loss at Port 2 (represented by the S_{22} plot in the green dashed line) exhibits a narrower bandwidth. This simulation result is reasonable since the feed positions are different: Port 1 was located at a corner of the hexagonal loop, while Port 2 was located at the midpoint of one side of the hexagonal loop. In addition, the port isolation (S_{21}, S_{12}) remains less than -15 dB in the 30–46 MHz band, which confirms good decoupling between the two ports. These results validate the suitability of the antenna for dual-polarization operation in the 34–46 MHz band.

To determine the polarization orientation of the antenna, the current distributions for both feed ports were analyzed. Figure 5 shows the surface current distribution and resulting electric field. For Port 1 excitation, strong currents flow along the lower and upper arms with zero at the left peak, creating an electric field directed upward along the y-axis. For Port 2 excitation, currents flow along the left and right arms with zero at the upper peak, producing an electric field in the orthogonal x-direction. These results confirm the formation of mutually orthogonal polarizations.

3. MEASUREMENT SETUP

3.1. S-Parameter Measurement Setup

S-parameter measurements were conducted using a Vector Network Analyzer (Anritsu MS46122B) with the configuration shown in Figure 6. Port 1 and Port 2 of the antenna were con-

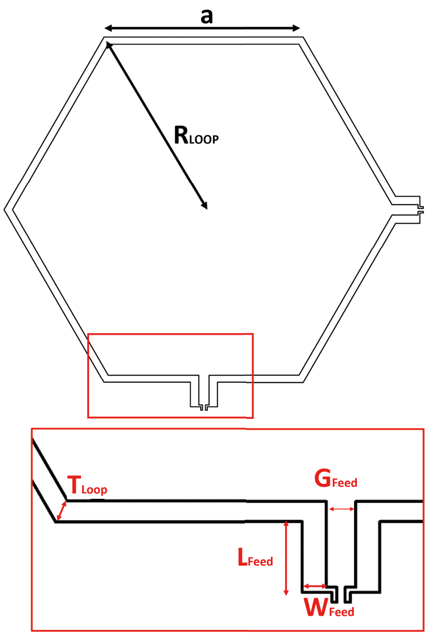

FIGURE 3. Detailed geometry model of the hexagonal loop antenna used in full-wave EM simulation, including feedline parameters T_{Loop}, G_{Feed}, L_{Feed}, and W_{Feed}.

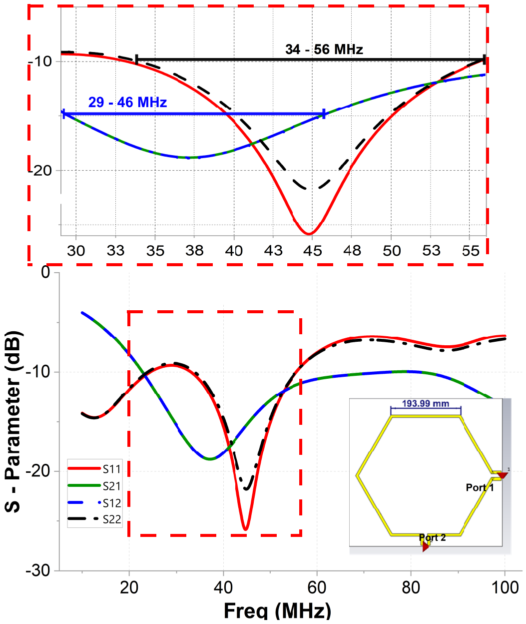

FIGURE 4. Simulated S-parameters (S_{11}, S_{21}, S_{12}, S_{22}) of the hexagonal loop antenna showing impedance bandwidth from 34–56 MHz.

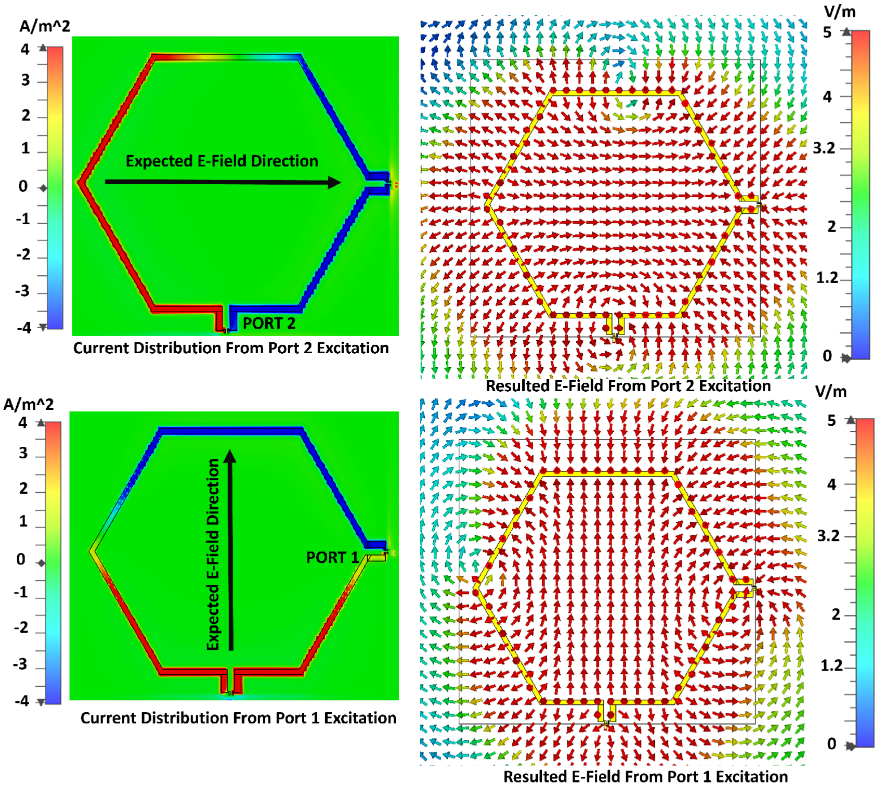

FIGURE 5. Simulated surface-current distribution and corresponding electric-field vectors for Port 1 and Port 2 excitation. The opposite current directions confirm orthogonal polarizations between the two ports.

nected to the corresponding VNA ports, which were calibrated across 10–100 MHz. During measurements, the S-parameters S_{11}, S_{12}, S_{21}, and S_{22} were recorded in both logarithmic magnitude (LogMag) and complex formats. LogMag data were used to evaluate reflection and isolation, while complex data were used to calculate the correlation coefficient between ports using Equation (8).

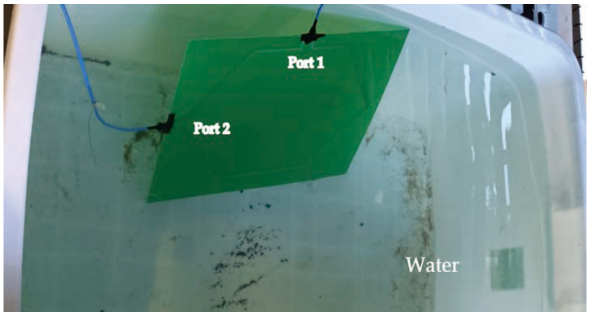

FIGURE 6. Experimental setup for underwater S-parameter measurement showing the dual-port antenna submerged in freshwater. The antenna is connected through waterproof coaxial cables to a calibrated VNA.

The Vector Network Analyzer (VNA) was calibrated using the standard full two-port Short-Open-Load-Thru (SOLT) method, identical to the procedure applied to antenna measurements in air. Calibration was performed at the SMA connector reference plane to ensure accurate impedance and scattering parameter readings. During underwater measurements, the coaxial extension cables and SMA connectors were sealed with waterproof compound to prevent water ingress while maintaining identical electrical reference conditions as in air calibration. This approach ensured that the underwater measurement results remained accurate and directly comparable with both simulations and air-based reference measurements.

Table 3 summarizes all experimental parameters, including physical dimensions of the water tank, environmental conditions, and measurement settings, to support reproducibility of the experiment.

TABLE 3. Experimental setup and environmental parameters for S-parameter measurement.

Parameter	Specification
Measurement location	Laboratory water tank
Tank dimensions ($L \times W \times H$)	$1048 \times 728 \times 559$ mm
Water type	Freshwater
Conductivity (σ)	0.0487 S/m
Relative permittivity (ε_r)	81
Water temperature	27°C (room temperature)
Antenna position	Fully submerged at mid-depth
Measurement instrument	VNA Anritsu MS46122B
Calibration method	Full two-port SOLT calibration
Frequency sweep range	10–100 MHz
Calibration reference plane	SMA-SMA 1.2 m RF Cable
Measurement precision	±0.05 dB amplitude, ±0.5° phase
Recorded data type	LogMag and complex

3.2. Radiation Pattern Characterization in Far-Field Setup

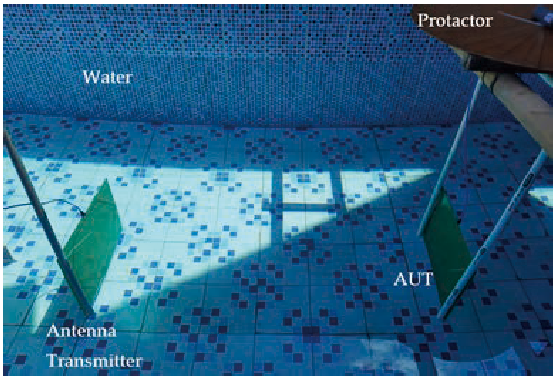

FIGURE 7. Photograph of the far-field radiation-pattern measurement setup conducted in a freshwater pool. The antenna under test (AUT) is positioned opposite the transmitting antenna with a controlled separation distance.

Radiation pattern measurements were carried out in a freshwater swimming pool with a depth of 1.4 meters. The antenna under test (AUT) was submerged at mid-depth and placed at a distance of 1.3 meters from the transmitting antenna, which remained fixed during all measurements. Waterproof sealant was applied to all connectors to prevent water seeping into the connector. The radiation pattern measurement setup has been set up and documented as shown in Figure 7.

For each measurement, the AUT was rotated horizontally (azimuthal sweep from 0° to 360°), while its elevation angle remained fixed. The step angle increment was 15°. Port 1 is assumed to generate horizontal polarization and Port 2 vertical polarization. Co- and cross-polarization patterns were obtained by switching the feeding ports of both AUT and the transmitting antenna. The S_{21} magnitude was recorded during the full sweep for each configuration.

3.3. Experimental Validation of Polarization Diversity under Dynamic Conditions

To verify the polarization diversity performance experimentally, a dynamic signal reception test was conducted. Prior to the diversity experiment, the actual output power of the USRP B210 transmitter was characterized to ensure accurate reference levels. The USRP B210 features a configurable numerical transmitting gain (0–50), whose corresponding actual power levels were measured using a spectrum analyzer through a Minicircuits 141-2MSM+ coaxial cable with insertion loss less than 0.25 dB. The measured power at a gain setting of 0 was -26 dBm, which was used for the underwater transmission test to minimize potential hardware stress and maintain stable performance. This characterization ensures that the experimental power levels reported in this study accurately reflect the real transmission conditions of the system.

A USRP B210 was used for both transmission and reception. The transmitter emitted a multitone signal centered at 40 MHz with an actual output power of approximately -26 dBm, corresponding to the minimum numerical gain setting of the USRP. This power level was selected to ensure stable operation and to prevent potential overdrive of the RF front-end during underwater experiments. The transmitting antenna (only single-port excitation) was randomly shaken and rotated by hand to simulate multipath fading and polarization fluctuation, as depicted

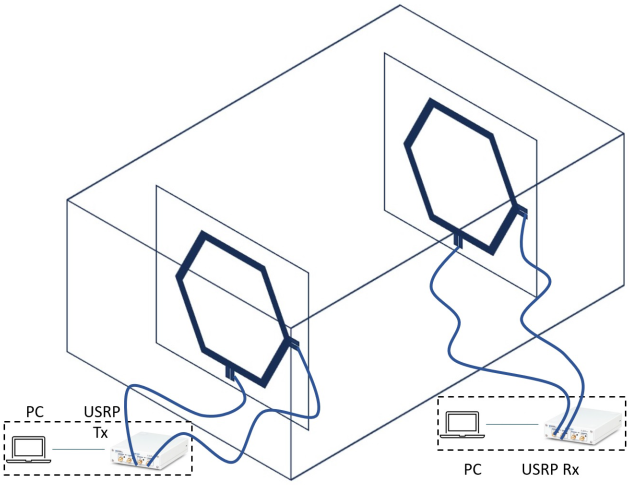

FIGURE 8. Experimental configuration for dynamic signal-reception test using dual-polarized hexagonal loop antennas connected to USRP B210 devices for transmission and reception, both controlled via PC-based LabVIEW software.

in Figure 8. This test approximates the behavior of a 2 × 2 MIMO channel, where independence between ports is important for diversity gain.

The received signals at both ports were continuously monitored and recorded using a LabVIEW program with user interface as shown in Figure 9. The fluctuations show that signal strength tends to alternate between ports, indicating that when one port receives a weak signal, the other often receives a stronger signal. This behavior significantly benefits performance for diversity-combining techniques.

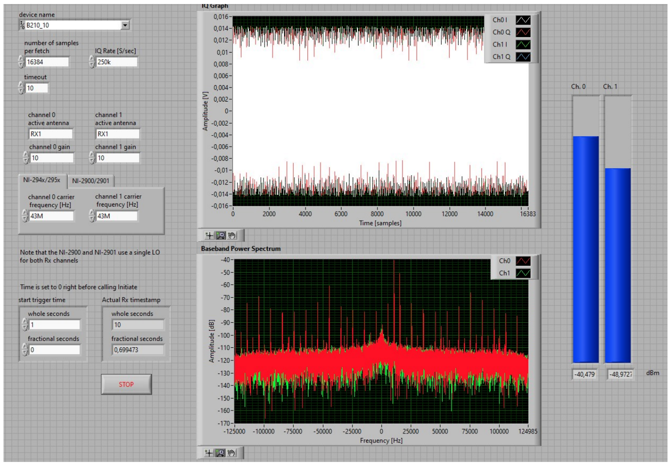
device name: B210_10
number of samples per fetch: 16384
IQ Rate [S/sec]: 250k
timeout: 10
channel 0 active antenna: RX1
channel 1 active antenna: RX1
channel 0 gain: 10
channel 1 gain: 10
channel 0 carrier frequency [Hz]: 43M
channel 1 carrier frequency [Hz]: 43M
Note that the NI-2900 and NI-2901 use a single LO for both Rx channels
Time is set to 0 right before calling Initiate
start trigger time: whole seconds: 1; fractional seconds: 0
Actual Rx timestamp: whole seconds: 10; fractional seconds: 0,699473
Ch. 0: -40,479 dBm
Ch. 1: -48,9727 dBm

FIGURE 9. Screenshot of the LabVIEW monitoring interface used during the polarization-diversity experiment. The two vertical bars on the right display the instantaneous received power at Port 1 and Port 2 (in dBm).

To evaluate the effectiveness of diversity techniques, the received power level data were analyzed using three combining methods: Selection Combining (SC), Maximal Ratio Combining (MRC), and Equal Gain Combining (EGC) with the formula as written in Equations (5) to (7).

$$\gamma_{\mathrm{SC}} = \max\left(\gamma_1, \gamma_2\right), \tag{5}$$

$$\gamma_{\mathrm{MRC}} = \gamma_1 + \gamma_2, \tag{6}$$

$$\gamma_{\mathrm{EGC}} = \left(\frac{\sqrt{\gamma_1} + \sqrt{\gamma_2}}{2}\right)^2, \tag{7}$$

It should be noted that the combining operations were implemented in the power domain, based on the received power (in dBm) independently recorded from Port 1 and Port 2. No complex (I/Q) combining was performed during the measurements; instead, SC, MRC, and EGC calculations were conducted offline after data acquisition using the recorded power values.

These techniques were compared to evaluate the improvement in signal-to-noise ratio (SNR) represented by the symbol γ in the equations, following the reference methods in [20–22]. However, since the noise floor of the measurement hardware remains constant across all scenarios, the statistical analysis in this study focuses on the received power levels instead. This approach still reflects the relative performance differences among SC, EGC, and MRC, while ensuring that the comparison is not biased by hardware-dependent noise characteristics.

4. MEASUREMENT RESULT AND DISCUSSION

4.1. S-Parameter

Figure 10 presents the measured antenna S-parameters. The results show that S_{11} and S_{22} are not identical. This is in fact due to the different feed positions. Port 1 is at the corner of the hexagonal loop, while Port 2 is at the midpoint of a side. The return loss measurements on Port 1 (S_{11}) show a wider bandwidth, with a return loss less than -10 dB in the frequency

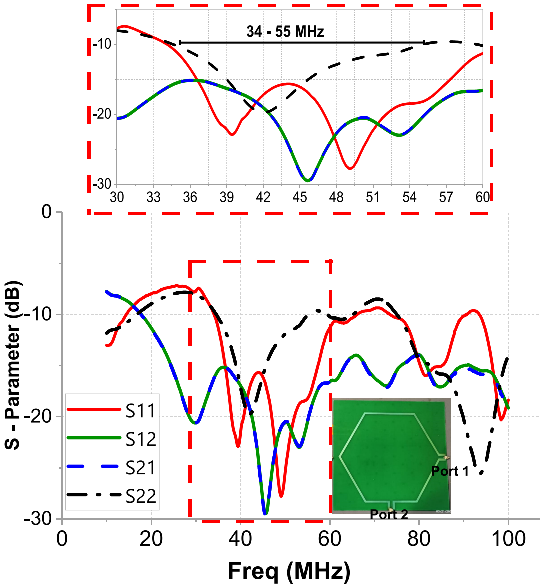

FIGURE 10. Measured S-parameters (S_{11}, S_{21}, S_{12}, S_{22}) of the fabricated dual-port antenna in freshwater. The measured impedance bandwidth spans 34–54 MHz, closely matching the simulated results shown previously. The inset photograph illustrates the prototype with indicated Port 1 and Port 2 locations.

range of 34–64 MHz. In contrast, Port 2 (S_{22}) shows a narrower bandwidth, with a return loss less than -10 dB in the frequency range of 35–54 MHz. This measurement result is consistent with the simulation results shown in Figure 4, where a minor impedance mismatch also causes S_{11} and S_{22} to differ slightly, although not as significantly as the measured results.

Moreover, the mutual coupling between the two ports, represented by S_{21} and S_{12}, is also critical in evaluating the performance of the dual-polarized configuration. The measurements indicate that S_{21} and S_{12} are identical and remain less than -15 dB across 30–60 MHz. It shows enough isolation between the ports. Based on these findings, the antenna achieves return loss less than -10 dB and inter-port isolation less than -15 dB in the frequency range of 34–55 MHz.

For dual-polarized antennas, it is important to verify that the two ports can operate independently. A key metric for this is the correlation coefficient, which is shown to be calculated from the S-parameters in complex format as described by Blanch et al. [23]. The correlation coefficient ρ is expressed as:

$$\rho = \frac{\left|S_{11}^{*} S_{12} + S_{21}^{*} S_{22}\right|^{2}}{\left(1 - |S_{11}|^{2} - |S_{21}|^{2}\right)\left(1 - |S_{22}|^{2} - |S_{12}|^{2}\right)} \tag{8}$$

where:

- S_{11}, S_{12}, S_{21}, and S_{22} are the measured scattering parameters.
- ρ is the resulting envelope correlation coefficient.

Figure 11 compares the measured and simulated correlation coefficients in the 10–100 MHz range. The measurement results (black curve) are slightly different from simulated values (red curve), but follow similar trends. The correlation coefficient remains less than 0.1 across the entire frequency range, indicating minimal mutual interaction between the two polarization ports. Within the 34–55 MHz band, both measured and simulated correlation coefficients are close to zero, demonstrating independent port and good isolation in the antenna's operating frequency band.

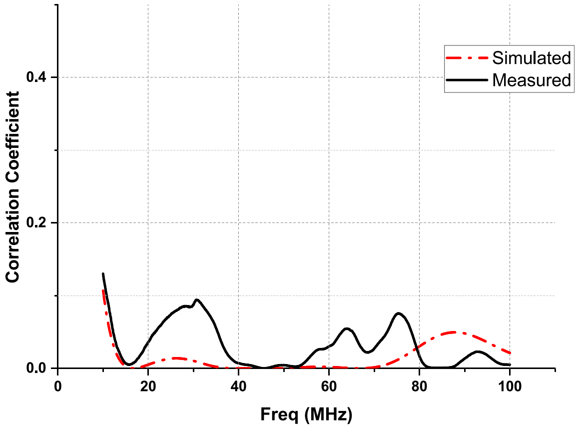

FIGURE 11. Comparison between simulated and measured envelope-correlation coefficients of the dual-polarized antenna, demonstrating low correlation (< 0.1) across the 34–56 MHz operating band.

Compared with the simulation results (Figure 4), the measured S-parameters in Figure 10 show a slight shift in resonance frequency and a variation in matching depth. Quantitatively, the simulated $|S_{11}|$ and $|S_{22}|$ below -10 dB occur within 34–56 MHz, while the measured range is 34–55 MHz with the S_{11} having a wider bandwidth than the simulation result. This deviation can primarily be attributed to the boundary effects of the limited water tank during the S-parameter measurement. The tank dimensions of $1048 \times 728 \times 559$ mm are comparable to the wavelength in freshwater ($\lambda \approx 0.735$ m), with the longest side about 1.43λ, the width about 0.99λ, and the height about 0.76λ. These proportions introduce additional reactive loading and coupling to the tank walls and water surface, which can shift the resonance by a few megahertz and modify the matching depth by several decibels. Interestingly, the measured port-to-port isolation (< -15 dB across 30–60 MHz) is slightly wider than simulated one (30–46 MHz), which is consistent with the altered propagation environment inside the tank.

In addition to the water tank boundary effect, several practical factors also contribute to observed discrepancies: (i) variation in epoxy coating thickness and uncertainty in the dielectric constant of both the epoxy and water medium, (ii) fabrication tolerances in conductor width, feed gap, and SMA soldering that change the effective loop inductance and capacitance, and (iii) underwater measurement artifacts such as the presence of waterproof sealant around connectors and minor cable movement that introduce parasitic capacitance and amplitude fluctuations on the order of a few tenths of a decibel.

To further analyze the dielectric influence of the protective epoxy layer, a parametric simulation was performed by varying the epoxy thickness from 0, 0.01, 0.1, and 1 mm, as illustrated in Figure 12. The fabricated prototype employs an ultra-thin epoxy coating of approximately 0.01 mm, primarily intended for surface sealing rather than structural reinforcement. The results indicate that for epoxy layers up to 0.1 mm, the return loss characteristics of Port 1 remain almost identical to those without coating, demonstrating negligible impedance detuning. This confirms that the thin epoxy layer does not significantly alter the effective dielectric loading or the surface current distribution along the loop conductor. Conversely, a thicker 1 mm

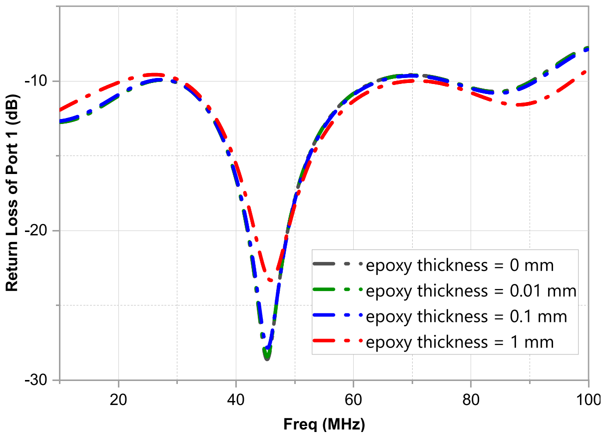

FIGURE 12. Simulated return-loss characteristics of Port 1 under different epoxy-coating thicknesses (0, 0.01, 0.1, and 1 mm). The results confirm that coatings up to 0.1 mm cause negligible impedance detuning, whereas a 1 mm layer introduces a minor frequency shift due to increased dielectric loading.

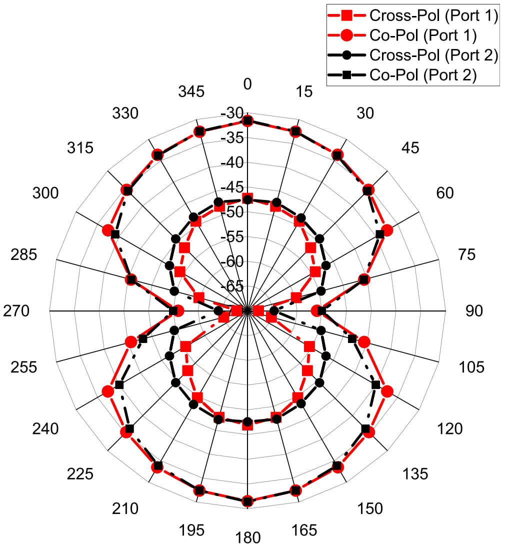

FIGURE 13. Measured far-field radiation patterns for Port 1 and Port 2 at the center frequency. Strong co-polarized components and low cross-polarization levels validate the orthogonal dual-polarization performance of the antenna.

coating introduces a minor frequency shift and slightly reduced return loss due to an increase in the effective permittivity surrounding the radiating structure. However, such thickness exceeds the actual fabrication condition and is therefore not practically relevant. These findings validate that a thin epoxy-coated antenna can be effectively used for underwater operation without requiring bulky waterproof housing, thus maintaining compactness while minimizing additional dielectric losses.

Overall, these combined effects are sufficient to account for the deviations between simulation and measurement, and the consistent trend of the S-parameter responses confirms the reliability of the design validation.

4.2. Far-Field Pattern

The measured far-field radiation patterns of the proposed dual-polarized hexagonal loop antenna are presented in Figure 13. The results demonstrate strong co-polarization (Co-Pol) and low cross-polarization (Cross-Pol) levels for both ports. An axial ratio of approximately 15 dB is observed in the main lobe (see Figure 14), indicating effective polarization isolation and confirming the dual-polarization capability of the antenna.

Port 1 radiates a horizontally polarized wave, while Port 2 radiates a vertically polarized wave. This polarization orthogonality is further supported by the simulated current distributions and electric field vectors shown in Figure 5.

For Port 1 excitation, the surface current is positive on the lower arm and negative on the upper arm of the hexagonal loop, producing a null at the left vertex. This configuration results in a y-directed electric field, which corresponds to horizontal polarization. In contrast, Port 2 exhibits positive currents on the left and right arms, with a null at the top vertex, generating an x-directed electric field consistent with vertical polarization.

These results validate the measured polarization characteristics. The alignment between the simulated and measured results provides evidence that the antenna structure supports orthogonal polarization modes with minimal mutual coupling, making it suitable for dual-polarization applications in underwater environments.

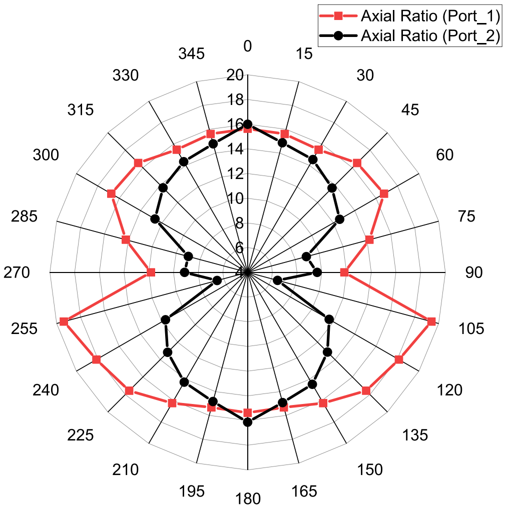

FIGURE 14. Measured axial-ratio patterns of Port 1 and Port 2, indicating an average axial ratio of approximately 15 dB within the main-lobe direction, confirming high polarization purity.

The orthogonality observed in the measured far-field patterns arises directly from the geometrical symmetry and feed placement of the hexagonal loop. Each port excites a pair of current paths oriented 90° apart, resulting in electric fields polarized along orthogonal axes, as confirmed in Figure 5. The equal loop length and symmetric arm configuration ensure that the two modes experience nearly identical impedance and radiation conditions, thereby minimizing polarization leakage and maintaining a low cross-polarization level. In the freshwater medium, characterized by $\varepsilon_r \approx 81$ and $\sigma \approx 0.0487\,\mathrm{S/m}$, the attenuation predominantly affects the overall field amplitude rather than the polarization state, since both orthogonal components undergo comparable dielectric and ohmic losses. This explains the consistent co-/cross-polarization ratios and the measured axial ratio about 15 dB, confirming that polarization purity is preserved even under lossy underwater conditions.

Building upon the above pattern evidence, the underlying electromagnetic mechanisms that govern the observed performance can be summarized as follows. The six-fold symmetry of the hexagonal loop, together with the orthogonal feed placement, excites two near-orthogonal surface-current modes whose magnetic-field axes are rotated by approximately 90°. Each port predominantly drives a current pair that encloses a magnetic loop normal to the opposite side of the structure, so the induced fields are naturally decoupled, and the cross-polarized component is minimized. This modal orthogonality explains the consistently low envelope-correlation coefficient ($\rho < 0.1$) and the inter-port isolation better than -15 dB observed in the measurements, and is also consistent with the simulated current vectors in Figure 5. In freshwater, characterized by $\varepsilon_r \approx 81$ and $\sigma \approx 0.0487\,\mathrm{S/m}$, attenuation is dominated by ohmic and dielectric losses that act almost uniformly on both orthogonal components; therefore, the lossy medium primarily

TABLE 4. Statistical summary of measured received power.

Scheme	Mean [dBm]	Std. Dev. [dB]	SE of Mean	95% CI [dBm]	Min [dBm]	Max [dBm]
Port 1	−54.18	5.00	0.039	[−54.26, −54.10]	−77.30	−45.47
Port 2	−54.12	4.94	0.039	[−54.20, −54.04]	−77.30	−45.68
SC	−50.78	1.98	0.015	[−50.81, −50.75]	−63.15	−45.47
MRC	−49.59	1.80	0.014	[−49.62, −49.56]	−62.83	−44.72
EGC	−50.21	1.92	0.015	[−50.24, −50.18]	−64.03	−44.88

reduces the magnitude of the radiated fields without disturbing their polarization states. This accounts for the measured co-/cross-polarization contrast and the $\sim$ 15 dB axial-ratio in the main lobe. Finally, the epoxy sealing used in the prototype is ultra-thin ($\sim$ 0.01 mm), so its dielectric loading is negligible for field formation along the loop; parametric simulations corroborate that coatings up to 0.1 mm do not detune the return loss or alter modal balance, which preserves polarization purity while enabling a compact, housing-free implementation.

Beyond the radiation pattern characteristics, the overall transmission performance was also analyzed to estimate the realized gain and radiation efficiency of the antenna under the same measurement conditions. To quantify the radiation efficiency, a two-antenna link measurement was performed in freshwater at $f = 42.5\,\text{MHz}$ with an antenna separation of $R = 1.3\,\text{m}$. The electromagnetic properties of the medium are $\varepsilon_r = 81$, $\sigma = 0.0487\,\text{S/m}$, $\mu = \mu_0$, and $\varepsilon = \varepsilon_0\varepsilon_r$. The complex propagation constant is expressed as in Equations (1), (2), and (3). From the equations, the attenuation constant and wavelength in water are $\alpha \approx 1.011\,\text{Np/m}$ and $\lambda = 2\pi/\beta \approx 0.778\,\text{m}$. The total channel loss, excluding antenna effects, is the sum of absorption and geometric spreading losses, which can be evaluated using the Friis formula [24]:

$$L_{\text{abs}} = 8.686\,\alpha R \approx 11.4\,\text{dB}, \tag{9}$$

$$L_{\text{spread}} = 20\log_{10}\left(\frac{4\pi R}{\lambda}\right) \approx 26.5\,\text{dB}, \tag{10}$$

yielding $L_{\text{chan}} = L_{\text{abs}} + L_{\text{spread}} \approx 37.9\,\text{dB}$. Using the measured transmission coefficient of $S_{21} = -31.6\,\text{dB}$ and assuming identical antennas, the realized gain per antenna follows

$$S_{21} = G_t + G_r - L_{\text{chan}} \Rightarrow 2G = S_{21} + L_{\text{chan}}, \tag{11}$$

resulting in $G \approx 3.13\,\text{dBi}$. With the measured directivity at 42.5 MHz of $D = 3.56\,\text{dBi}$, the radiation efficiency is

$$\eta = 10^{(G-D)/10} \approx 10^{(3.13-3.56)/10} = 0.905(90.5\%). \tag{12}$$

4.3. Experimental Verification of Polarization Diversity Performance

To evaluate the effectiveness of polarization diversity, an experimental analysis was performed using a dual-polarized antenna system, as described in Section 3.3. The received signal power levels were captured and recorded from two orthogonal polarization ports, CH0 (Port 1) and CH1 (Port 2), resulting in more than 16,000 samples.

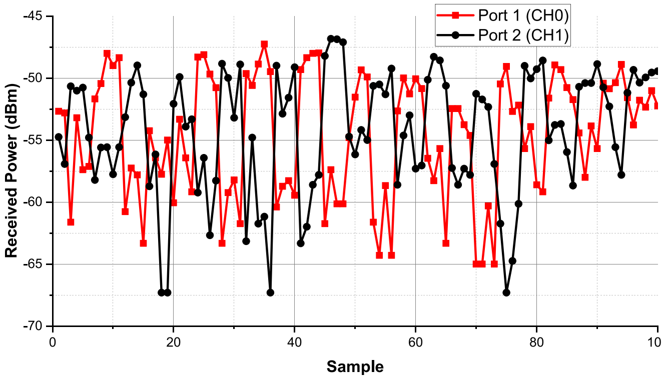

FIGURE 15. Time-varying received power at Port 1 (CH0) and Port 2 (CH1) recorded during the dynamic motion test. The alternating power levels between ports demonstrate polarization diversity under multipath fading conditions.

As a preliminary observation, Figure 15 illustrates the fluctuation in signal amplitude over the first 100 samples at both ports. Clearly, both Port 1 and Port 2 exhibit significant variation in signal amplitude over time, and the fluctuation patterns between the two ports are not identical. This provides evidence that the received signals are not fully correlated. Such partial de-correlation is important for polarization diversity, as it allows different fading characteristics to be exploited to improve signal reconstruction and reliability.

To quantify the gain obtained from polarization diversity, we analyzed the distribution of received power level across all 16,000 samples. The analysis includes individual received power levels from Port 1 and Port 2, as well as combined received power levels using three signal combining techniques: Selection Combining (SC), Equal Gain Combining (EGC), and Maximal Ratio Combining (MRC). The resulting distribution of received power levels is shown in Figure 16.

To strengthen the statistical validity of the experimental results, the mean received power, standard deviation, and 95% confidence intervals (CI) were computed based on more than 16,000 samples for each scheme, as summarized in Table 4 and can be seen in Figure 17. The resulting 95% CI values are notably narrow (less than ±0.05 dB), indicating a high degree of statistical confidence and measurement repeatability.

The standard deviation values for Port 1 and Port 2 are significantly larger (around 5 dB) than those of the diversity combining schemes. This behavior is expected since the experiment intentionally employed randomly generated polarization states at the transmitter to emulate time-varying polarization mismatch

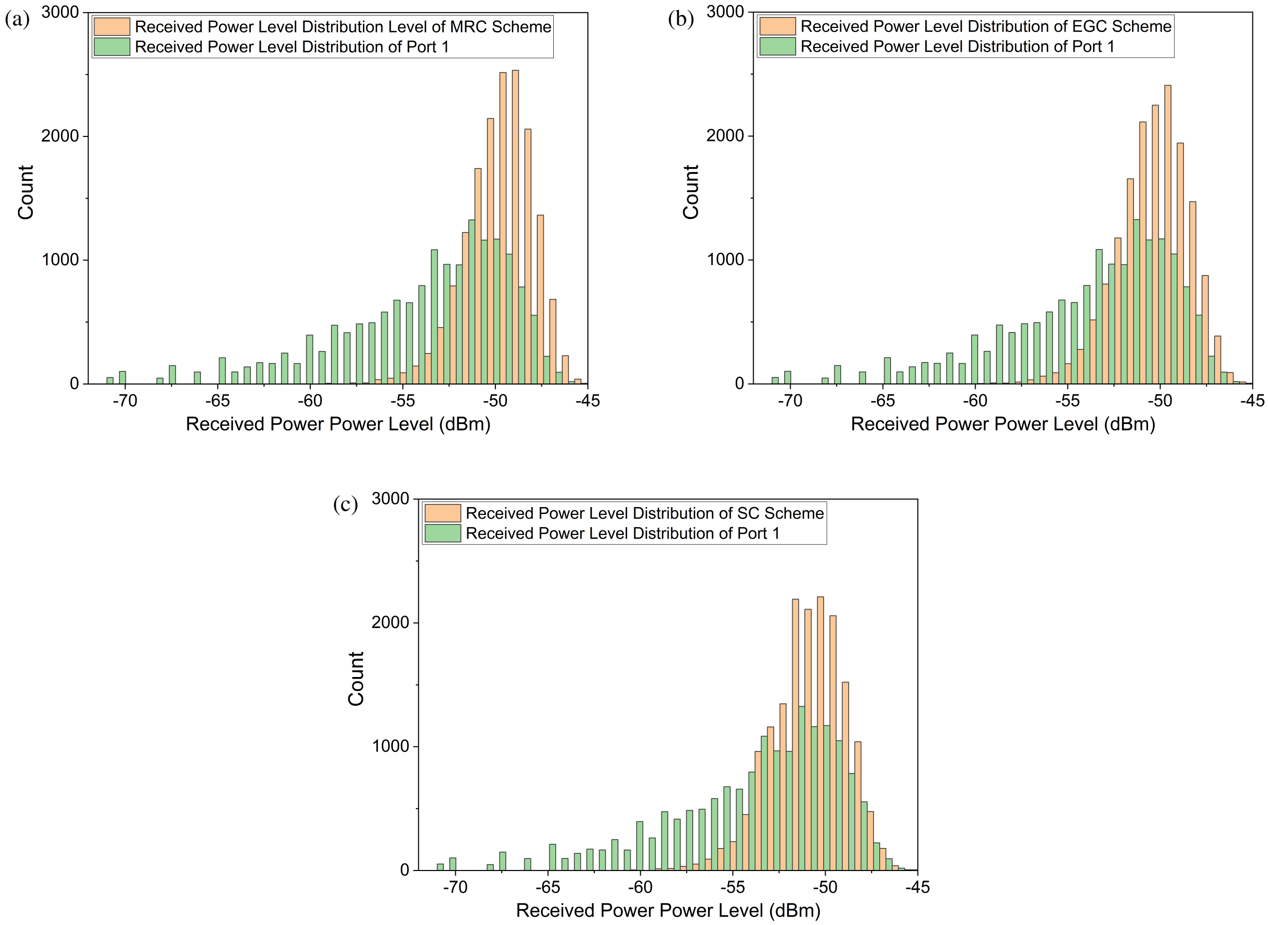

FIGURE 16. (a) Power-level distribution of MRC versus Port 1, (b) EGC versus Port 1, and (c) SC versus Port 1. All combining schemes exhibit a rightward shift compared to single-port reception, confirming diversity gain in average received power.

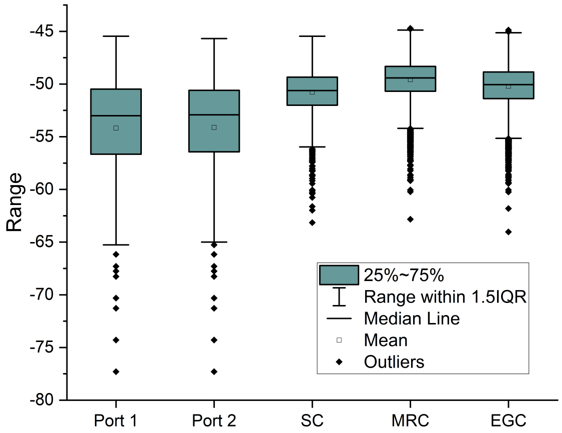

FIGURE 17. Statistical report of received power measurement on Port 1, Port 2 and all combining schemes.

conditions. Consequently, the instantaneous received power at each single port fluctuated substantially depending on the polarization alignment between the transmitter and receiver. In contrast, the diversity combining schemes (SC, EGC, and MRC) effectively mitigated these variations by jointly exploiting both polarization channels, which resulted in much smaller standard deviations (approximately 2 dB) and more stable received power distributions. A standard deviation around 2 dB is considered relatively small in this measurement context, indicating that the received power levels were stable, and the combining algorithms consistently enhanced the effective signal strength.

Moreover, the small deviations observed in the combining schemes confirm that the higher average received power is not caused by random fluctuations but represents a statistically consistent polarization diversity gain. Figure 18 further illustrates the mean received power with 95% CI error bars. The results clearly show the progressive enhancement from single-port reception (Port 1 and Port 2) to diversity combining techniques (SC, EGC, and MRC), with MRC achieving the highest average power and the smallest variance.

Among the combining methods, MRC achieves the highest performance gain, both in terms of average received power level and distribution sharpness. This result aligns with theoretical expectations, as MRC optimally weights the received signals based on their individual received power level contributions.

Overall, both the signal fluctuation patterns and statistical received power level distributions validate the effectiveness of polarization diversity in enhancing signal quality. The experiment provides evidence that dual-polarized antennas, when being combined with advanced combining methods, can signifi-

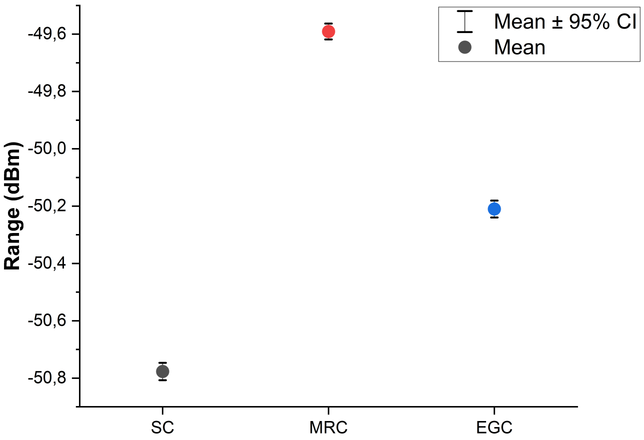

FIGURE 18. Comparison of mean received power levels with 95% confidence intervals for SC, MRC, and EGC combining schemes. The MRC method provides the highest mean received power, demonstrating the best diversity performance.

cantly improve the robustness and reliability of wireless communication systems.

5. CONCLUSION

This paper has presented the design, fabrication, and experimental validation of a compact dual-polarized hexagonal loop antenna for underwater communication at 40–45 MHz. Unlike prior studies that focused primarily on single-polarized or large-scale loop configurations, the proposed antenna introduces a practical dual-polarization geometry that enables polarization diversity in low-frequency underwater environments. By employing FR-4 substrate with epoxy resin coating, the antenna eliminates the need for bulky waterproof housings while maintaining reliable performance.

The measured results confirmed good impedance matching with return loss values below -10 dB and inter-port isolation consistently better than -15 dB, while the envelope correlation coefficient remained below 0.1 across the operating band of 34–55 MHz. Far-field radiation measurements demonstrated clear orthogonality between the two polarizations, validating the independent operation of both ports. Most importantly, experimental evaluation of diversity combining showed significant performance enhancement: selection combining, equal gain combining, and maximal ratio combining improved the average received power by 3.40 dB, 3.96 dB, and 4.59 dB, respectively, compared with single-port reception.

These findings establish, for the first time, the feasibility of a compact hexagonal dual-polarized antenna for underwater applications with experimentally verified polarization diversity. The demonstrated robustness against polarization fluctuations highlights the antenna's potential as a fundamental building block for future low-frequency MIMO-like systems in underwater wireless sensor networks, autonomous vehicle communications, and related marine applications. Future work will extend this study toward seawater environments, material optimization, and integration into multi-antenna communication platforms.

ACKNOWLEDGEMENT

The authors thank the School of Electrical Engineering and Informatics, Bandung Institute of Technology, for supporting this research.

REFERENCES

[1] Hasaba, R., K. Eguchi, T. Wakisaka, J. Hirokawa, M. Hirose, T. Matsushima, Y. Fukumoto, Y. Nishida, and K. Ishii, "Wavelet OFDM wireless communication system for autonomous underwater vehicles using loop-shaped antennas in underwater environments," *IEEE Access*, Vol. 12, 129 633–129 645, 2024.

[2] Lim, C. P., L. W. Li, and M. S. Leong, "Method of moments analysis of electrically large thin hexagonal loop transceiver antennas: Near- and far-zone fields," *Progress In Electromagnetics Research*, Vol. 30, 251–271, 2001.

[3] Patel, U., V. Purohit, and S. Shastri, "Comparative study of hexagonal and circular large loop antenna," in *2012 Nirma University International Conference on Engineering (NUiCONE)*, 1–6, Ahmedabad, India, 2012.

[4] Kawamura, T., T. Matsushita, T. Kondo, F. Takeuchi, K. Hongo, Y. Matsui, T. Takinami, A. Horii, and K. Ohkuri, "Design of a circularly polarized underwater antenna and its experimental verification using a water tank," in *2023 17th European Conference on Antennas and Propagation (EuCAP)*, 1–5, Florence, Italy, 2023.

[5] Amit, S. V., "Design and fabrication of a patch antenna for underwater communications," *Wireless Personal Communications*, Vol. 126, No. 3, 2671–2687, 2022.

[6] Dala, A. and T. Arslan, "Design, implementation, and measurement procedure of underwater and water surface antenna for Lora communication," *Sensors*, Vol. 21, No. 4, 1337, 2021.

[7] Inácio, S. I., M. R. Pereira, H. M. Santos, L. M. Pessoa, F. B. Teixeira, M. J. Lopes, O. Aboderin, and H. M. Salgado, "Antenna design for underwater radio communications," in *OCEANS 2016 — Shanghai*, 1–6, Shanghai, China, 2016.

[8] Paillette, T. D., A. Gaugue, E. Parlier, and S. Dardenne, "Antenna design for underwater wireless telemetry systems," in *2017 11th European Conference on Antennas and Propagation (EUCAP)*, 2251–2255, Paris, France, 2017.

[9] Aboderin, O., S. I. Inácio, H. M. Santos, M. R. Pereira, L. M. Pessoa, and H. M. Salgado, "Analysis of J-pole antenna configurations for underwater communications," in *OCEANS 2016 MTS/IEEE Monterey*, 1–5, Monterey, CA, USA, 2016.

[10] Santos, M. O., S. M. M. Faria, and T. R. Fernandcs, "Real time underwater radio communications in swimming training using antenna diversity," in *2021 Telecoms Conference (ConfTELE)*, 1–5, Leiria, Portugal, 2021.

[11] Feng, B., S. Qi, X. Ding, X. Yang, and C.-Y.-D. Sim, "A dual-polarized multi-wideband ceiling antenna with eight-diagram shape for 2G/3G/LTE/5G sub-6 GHz indoor applications," *IEEE Access*, Vol. 12, 135 338–135 351, 2024.

[12] Wu, S. and F. Shang, "Broadband dual-polarized magnetoelectric dipole antenna with compact structure for 5G base station," *IEEE Access*, Vol. 11, 20 806–20 813, 2023.

[13] Lin, Y.-F., C.-C. Chang, C.-H. Chen, J.-Y. Xie, Y.-X. Zhuang, and H.-M. Chen, "Dual-polarized spline-loop antenna array with tilt angle radiation for 5G base stations," *IEEE Access*, Vol. 12, 138 280–138 290, 2024.

[14] El Yousfi, A., K. A. Abdalmalak, A. Lamkaddem, A. M. Barrera, B. Biscontini, and D. Segovia-Vargas, "Miniaturized dual-polarized, high-gain, and wideband dielectric resonator antenna

for low band massive MIMO applications," *Progress In Electromagnetics Research*, Vol. 179, 101–111, 2024.

[15] Che, X., I. Wells, G. Dickers, P. Kear, and X. Gong, "Re-evaluation of RF electromagnetic communication in underwater sensor networks," *IEEE Communications Magazine*, Vol. 48, No. 12, 143–151, Dec. 2010.

[16] Aboderin, O., L. M. Pessoa, and H. M. Salgado, "Wideband dipole antennas with parasitic elements for underwater communications," in *OCEANS 2017 — Aberdeen*, 1–6, Aberdeen, UK, 2017.

[17] Cheng, D. K., *Field and Electromagnetics*, Addisson-Wesley, 1983.

[18] Balanis, C. A., *Antenna Theory: Analysis and Design*, 4th ed., John Wiley & Sons, Hoboken, NJ, 2016.

[19] Hao, J., K. Yang, J. Wu, M. Wu, and Y. Li, "Overview of recent developments in composite epoxy resin in organic coating on steel (2020-2024)," *Materials*, Vol. 18, No. 7, 2025. [Online]. Available: https://www.mdpi.com/1996-1944/18/7/1531.

[20] Goldsmith, A., *Wireless Communications*, Cambridge University Press, Cambridge, UK, 2005.

[21] Brennan, D. G., "Linear diversity combining techniques," *Proceedings of the IRE*, Vol. 47, No. 6, 1075–1102, Jun. 1959.

[22] Proakis, J. G. and M. Salehi, *Digital Communications*, 5th ed., 852–860, McGraw-Hill, New York, NY, USA, 2008.

[23] Blanch, S., J. Romeu, and I. Corbella, "Exact representation of antenna system diversity performance from input parameter description," *Electronics Letters*, Vol. 39, No. 9, 705–707, 2003.

[24] Jaafar, A. N. B., H. Ja'Afar, Y. Yamada, N. H. A. Rahman, N. Michishita, N. Zainudin, F. Sadeghikia, and R. Abdullah, "Electromagnetic analysis of radio propagation in fresh water and measurement by axial mode helical antenna at 433 MHz," *IEEE Open Journal of Antennas and Propagation*, Vol. 6, No. 4, 1112–1125, 2025.